Magnetic Resonance in Medicine 51:158–164 (2004)

Momentum-Weighted Conjugate Gradient Descent Algorithm for Gradient Coil Optimization

Hanbing Lu, Andrzej Jesmanowicz, Shi-Jiang Li, and James S. Hyde*

MRI gradient coil design is a type of nonlinear constrained optimization. A practical problem in transverse gradient coil design using the conjugate gradient descent (CGD) method is that wire elements move at different rates along orthogonal directions (r, φ, z), and tend to cross, breaking the constraints. A momentum-weighted conjugate gradient descent (MW-CGD) method is presented to overcome this problem. This method takes advantage of the efficiency of the CGD method combined with momentum weighting, which is also an intrinsic property of the Levenberg-Marquardt algorithm, to adjust step sizes along the three orthogonal directions. A water-cooled, 12.8 cm inner diameter, three axis torque-balanced gradient coil for rat imaging was developed based on this method, with an efficiency of 2.13, 2.08, and 4.12 $mT \cdot m^{-1} \cdot A^{-1}$ along X, Y, and Z, respectively. Experimental data demonstrate that this method can improve efficiency by 40% and field uniformity by 27%. This method has also been applied to the design of a gradient coil for the human brain, employing remote current return paths. The benefits of this design include improved gradient field uniformity and efficiency, with a shorter length than gradient coil designs using coaxial return paths. Magn Reson Med 51:158–164, 2004.

Key words: gradient coil; conjugate gradient descent; Levenberg-Marquardt algorithm; coil efficiency; field uniformity

Gradient coils with high efficiency and fast slew rate are desirable in a variety of MRI applications, and a local gradient coil is an efficient way to meet these requirements. There are two classes of methodologies in local gradient coil design: analytical approaches and numerical optimization methods (1). For coil design using analytical approaches, the geometry of the coil usually needs to be defined, which is inconvenient when the geometry is not easily handled or the optimum geometry is unknown, such as the "sandwich" coil design (2). In the sandwich geometry, remote current return paths are used to design a short local gradient coil for human brain imaging; wire elements are embedded in circular disks and sandwiched together. The optimum surface geometry for the wire elements is unknown. Numerical optimization methods can be advantageous in these cases (3–9). Conjugate gradient descent (CGD) is an established numerical optimization method. It was introduced for gradient coil and RF coil optimization by Wong et al. (3), and subsequently applied to gradient coil design by Brey et al. (9) and others. In the context of MRI, this method has also been applied to RF pulse optimization (10) and image reconstruction for parallel imaging (11).

The attractive feature of CGD is its flexibility. A desired field in the region of interest (ROI) of any shape can be arbitrarily prescribed, constraints on current elements can be easily applied, and the error functions can be flexibly combined with field uniformity, inductance, and power consumptions. This process can be combined with other coil design methods for final optimization.

In the past, with gradient coils optimized using the CGD method (3,9), the variables to be optimized were either the currents at prescribed locations or the locations for prescribed currents. For a design to be practical for construction, there are several constraints. They include: 1) current is continuous; 2) the space between neighboring wires should be greater than defined minimum values; 3) the wire elements must be within defined physical dimensions of the coil; and 4) there is no crossover of wires. These constraints are readily satisfied when the variable to be optimized is one-dimensional. For example, for a Z gradient coil on a cylindrical surface, the variables to be optimized are the positions of the wire loops with constant diameters. Only the z coordinates need to be optimized (in cylindrical coordinates (r, φ, z)).

However, there are conditions where the coordinates to be optimized are multidimensional, including the transverse gradient coil design on a cylindrical surface, where both the φ and z locations need to be optimized for each wire. Another example is the sandwich gradient coil design, where r, φ, and z coordinates must be optimized. A practical consideration is that each element moves at significantly different rates along the three orthogonal directions (r, φ, z), and neighboring elements tend to cross, breaking the constraints listed above. This limits the number of wire elements that can be employed, degrades coil efficiency and gradient field uniformity, and can result in designs that are impractical for construction. This problem was encountered during the design of a high-efficiency transverse gradient coil for animal studies and a sandwich gradient coil for the human brain. To the best of our knowledge, this problem has not been fully addressed in the literature of MRI gradient coil design.

The purpose of this work is to develop a method to mitigate this problem. Theoretical analysis is presented, followed by experimental results. Our approach enabled practical designs to be generated with improved coil efficiency and field uniformity. Preliminary accounts of the present work have been presented elsewhere (2,12). This method may be useful in other numerical optimization environments.

Department of Biophysics, Medical College of Wisconsin, Milwaukee, Wisconsin.

Grant sponsor: National Institutes of Health; Grant numbers: EB002014; EB000215.

*Correspondence to: Prof. J.S. Hyde, Department of Biophysics, Medical College of Wisconsin, 8701 Watertown Plank Road, Milwaukee, WI 53226. E-mail: jshyde@mcw.edu

Received 9 June 2003; accepted 27 August 2003.

DOI 10.1002/mrm.10662
Published online in Wiley InterScience (www.interscience.wiley.com).

MATERIALS AND METHODS

General Theory

For a multivariable function, $f(x)$ at $\boldsymbol{p}$ can be approximated by a Taylor series, given by:

$$f(x) = f(\boldsymbol{p}) + \sum_k \frac{\partial f}{\partial x_k} x_k + \frac{1}{2} \sum_{k,l} \frac{\partial^2 f}{\partial x_k \partial x_l} x_k x_l + \cdots$$

$$\approx c + \boldsymbol{b} \cdot \boldsymbol{X} + \frac{1}{2} \boldsymbol{X} \cdot \boldsymbol{A} \cdot \boldsymbol{X}$$

$$\text{where } c = f(\boldsymbol{p}),\ \boldsymbol{b} = \nabla f\Big|_{\boldsymbol{p}},\ [\boldsymbol{A}]_{k,l} = \frac{\partial^2 f}{\partial x_k \partial x_l}\Big|_{\boldsymbol{p}}. \qquad [1]$$

Here, $\boldsymbol{A}$ is the Hessian matrix whose components $A_{k,l}$ are the second-order partial derivatives of $f(x)$ at $\boldsymbol{p}$, and $\boldsymbol{b}$ is the first-order partial derivative matrix of $f(x)$ at $\boldsymbol{p}$. The local minimum of $f(x)$ can be found iteratively using CGD based on the method described in Ref. 13.

In gradient coil optimization, the error function can be defined as:

$$E = \sum_{m=1}^{M} (B_m - \bar{B}_m)^2, \qquad [2]$$

where $\bar{B}_m$ is the desired magnetic field at the mth point in the ROI, B_m is the calculated magnetic field at this point using the Biot-Savart law, and M is the total number of specified points in the ROI. It is apparent that E is a function of the coordinates of the wire elements. In gradient coil optimization, the challenge is to find the optimum coordinates for each of the wire elements $p_0, p_1, p_2, \ldots, p_N$, such that the error function E is minimized under the constraints.

The gradient vector for the nth element can be calculated using the finite difference of the error function, given by:

$$\frac{\partial E}{\partial r_n} = \frac{2 \sum_{m=1}^{M} (B_m - \bar{B}_m) \cdot \partial B_m}{\partial r_n}, \qquad [3a]$$

$$\frac{\partial E}{r_n \cdot \partial \varphi_n} = \frac{2 \sum_{m=1}^{M} (B_m - \bar{B}_m) \cdot \partial B_m}{r_n \cdot \partial \varphi_n}, \qquad [3b]$$

$$\frac{\partial E}{\partial z_n} = \frac{2 \sum_{m=1}^{M} (B_m - \bar{B}_m) \cdot \partial B_m}{\partial z_n}. \qquad [3c]$$

The local minima of $\boldsymbol{E}$ can be searched iteratively using the CGD method. Specifically, at the ith iteration, the search direction for the nth element ($dr_{n,i}$, $d\varphi_{n,i}$, $dz_{n,i}$) can be derived based on the method described in Refs. 3 and 13 using the gradient vectors described above. The coordinates of the wire elements are optimized using the following equation:

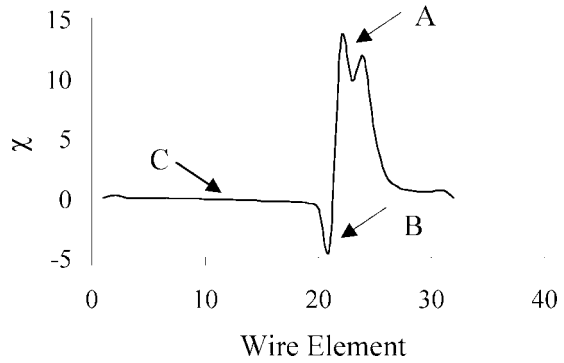

FIG. 1. The χ values in the wire elements along half of a loop (the other half is symmetric), where χ is defined in Eq. [5]. *A* and *B* indicate elements with large χ values, and *C* indicates $\chi \approx 0$.

$$\boldsymbol{P}_{i+1} = \boldsymbol{P}_i + \xi \boldsymbol{d}_i, \qquad [4]$$

where $\boldsymbol{P}$ and $\boldsymbol{d}$ are N-dimensional vectors representing the coordinates of the wire elements and the search directions, respectively. ξ is the step size to be chosen to minimize E along direction $\boldsymbol{d}$.

For convenience, we chose cylindrical coordinates for the calculations. In practice, the numerical values of $\partial E/(r_n \cdot \partial \varphi_n)$ and $\partial E/\partial z_n$ are dramatically different between wire loops, and between segments within the same loop, depending on optimization stages. The ratio of $\partial E/(r_n \cdot \partial \varphi_n)$ over $\partial E/\partial z_n$ is introduced to address this problem:

$$\chi_n = \frac{\partial E/(r_n \cdot \partial \varphi_n)}{\partial E/\partial z_n} \qquad [5]$$

Figure 1 shows the χ values in a wire loop during the optimization of a transverse gradient coil on a cylindrical surface (only half of this loop is shown because of symmetry). In this case, r_n is the radius of the cylinder (R).

$$\begin{aligned} &\chi \in [0.013,\ 0.048] && \text{for } 1 \le n \le 18, \\ &\chi_{\min} = -4.339 && \text{for } n = 21, \\ &\chi_{\max} = 13.321 && \text{for } n = 22. \end{aligned}$$

Two observations can be made: first, the absolute values of χ are not close to one. They are close to zero in region *C* (see Fig. 1), and are higher in *A* and *B*. Variations of about 1000 times exist. Second, the local minima and maxima of the χ values are closely spaced. The local maximum points are at n = 22 and 24, and local minimum points are at n = 21 and 23. These data indicate that the curvature of the error surface is strongly "valleyed" at the locations where χ values are close to zero (in region *C*), and that the error surface is not flat where peak χ values alternate (in regions *A* and *B*). Similar phenomena were found in the sandwich gradient coil design. In this case, peak $\partial E/\partial z \gg$ peak $\partial E/(a \cdot \partial \varphi) \gg$ peak $\partial E/\partial r$, where a is the radius of the inner circle.

In coil optimization using CGD as developed by Wong et al. (3), only the first-order partial derivatives are used. The second-order partial derivatives (the Hessian matrix), which encode the *curvature* information of the error function, are not used. The curvature of the error surface makes

wire elements move at different rates along different directions in vector space and tend to cross, limiting the number of wire loops that can be employed. This degrades coil efficiency and field uniformity.

Levenberg-Marquardt Method

The Levenberg-Marquardt method (13–16) can be used, in principle, to address this problem. This method estimates the Hessian matrix using the first-order partial derivatives and performs the optimization based on the following equation:

$$\boldsymbol{P}_{i+1} = \boldsymbol{P}_i - (\boldsymbol{H} + \lambda \cdot diag[\boldsymbol{H}])^{-1} \cdot \boldsymbol{d}_i, \quad [6]$$

where $\boldsymbol{d}$ is the search direction and $\boldsymbol{H}$ is the approximated Hessian matrix, formed from the first-order partial derivatives (13,14). This method adjusts step size for each parameter, based on the estimated Hessian matrix. When λ is a large number or $\boldsymbol{H}$ is set to be an identity matrix, Eq. [6] has a steep descent. In essence, this method moves farther in the directions with smaller gradients and less in the directions with larger gradients in order to get around the classic "error valley" problem. This algorithm involves a matrix inversion, which is a minor issue for Z gradient coil optimization. However, for the example of transverse gradient coil optimization that we address, the matrix size is 1280 $\times$ 1280, and iterative matrix inversion would be computationally intensive.

Momentum-Weighted CGD (MW-CGD) Method for Transverse Gradient Coil Design

Since large differences exist in the gradients along the radial, azimuthal, and z directions as shown in Fig. 1, a practical approach has been developed that combines the efficiency of CGD with weightings that are analogous to those of the Levenberg-Marquardt algorithm. Specifically, Eq. [4] is decomposed into the following equation:

$$\begin{bmatrix} r_{0,i+1} & \varphi_{0,i+1} & z_{0,i+1} \\ r_{1,i+1} & \varphi_{1,i+1} & z_{1,i+1} \\ \cdots & & \\ r_{N,i+1} & \varphi_{N,i+1} & z_{N,i+1} \end{bmatrix} = \begin{bmatrix} r_{0,i} & \varphi_{0,i} & z_{0,i} \\ r_{1,i} & \varphi_{1,i} & z_{1,i} \\ \cdots & & \\ r_{N,i} & \varphi_{N,i} & z_{N,i} \end{bmatrix} + \alpha_i \cdot \begin{bmatrix} dr_{0,i} & d\varphi_{0,i} & dz_{0,i} \\ dr_{1,i} & d\varphi_{1,i} & dz_{1,i} \\ \cdots & & \\ dr_{N,i} & d\varphi_{N,i} & dz_{N,i} \end{bmatrix} \cdot \begin{bmatrix} \beta & 0 & 0 \\ 0 & \gamma & 0 \\ 0 & 0 & 1 \end{bmatrix} \quad [7]$$

where α_i is the step size along z at the ith iteration, and β and γ are defined according to the following three conditions:

(i) for a cylindrical Z gradient coil design, $\beta = \gamma = 0$.
(ii) for a cylindrical transverse gradient coil design, $\beta = 0$, and γ is defined as:

$$\gamma = \frac{1}{N} \sum_{n=1}^{N} [(\partial E/\partial z_n)/(\partial E/R \cdot \partial \varphi_n)]^2, \quad [8a]$$

(iii) for a coil design on an irregular surface, such as a sandwich gradient coil design, γ is similar to Eq. [8a] and β is defined as:

$$\beta = \frac{1}{N} \sum_{n=1}^{N} [(\partial E/\partial z_n)/(\partial E/\partial r_n)]^2. \quad [8b]$$

Here β and γ provide momentum weightings of the step sizes for the radial and azimuthal coordinates.

The parameter α is chosen based on the following procedures: At the ith iteration, the error function $E(\mathbf{P}_i)$ is calculated. Parameter α starts with a small number, say 0.0001; $\boldsymbol{P}_{i+1}$ is derived using Eqs. [7], [8a], and [8b]; and error function $E(\mathbf{P}_{i+1})$ is evaluated. Parameter α is successively doubled or halved until the following condition is satisfied:

$$\frac{E(\boldsymbol{P}_i) - E(\boldsymbol{P}_{i+1})}{E(\boldsymbol{P}_i)} \leq \zeta, \quad [9]$$

where ζ is an empirical number that determines the amount of error decrease at each iteration. In our experience, ζ is usually good if the error decreases about 5–10% (ζ is between 0.05 and 0.1). The error function is usually minimized under the constraints after 20–30 iterations. During the early stages of optimization, α is typically small. The effects of a small α are twofold: it ensures that the quadratic approximation of the error function is valid, and it also enhances the effects of momentum weighting, since the amplitude of the gradients tends to be large during the early stages.

RESULTS

Gradient Coil Design for Rat Imaging

We have applied this method to the design of a three-axis torque-balanced cylindrical gradient coil for rat imaging. A 12.8 cm inner diameter was chosen to permit enough space for placing stimulus and physiological monitoring equipment inside the coil for fMRI using small animals. The ROI to be optimized was a sphere of 7 cm diameter at the center of the coil. Eighty points (M = 80) within one octant of the sphere were defined as the discrete ROI. The desired magnetic field at each point ($\bar{B}_m$) was specified. An initial pattern of 20 loops with 128 segments in each loop was also prescribed. The magnetic field at each point of the ROI (B_m) was calculated. The error function was defined based on Eq. [2]. A total of 1280 wire segments, each with two variables (φ and z), needed to be optimized. The goal was to optimize the coordinates of these wire segments so that the error function was minimal under the constraints. The prescription of the initial pattern was somewhat arbitrary. However, after 2–3 trials, an initial pattern could be readily prescribed. In our experience, the final pattern did not depend strongly on the initial pattern, since a "bad" initial pattern could be corrected during the optimization stages that followed.

The optimization process was carried out as follows: the first-order partial derivatives were calculated using Eqs. [3a]–[3c]. Search direction $\boldsymbol{d}$ for the wire segments was derived

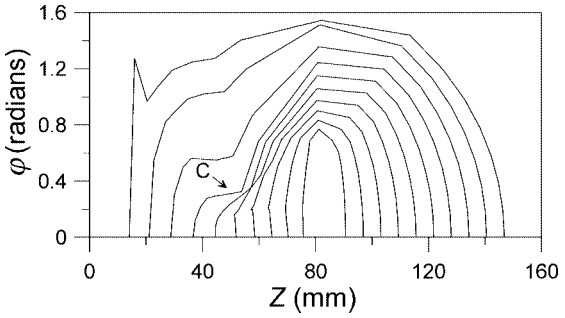

FIG. 2. One octant of the winding patterns without using the proposed method. *D* indicates the sharp inflections in the winding pattern. These inflections limit the number of winding loops that can be employed (only 10 winding loops were able to be incorporated in this case), which degrades the coil efficiency and gradient field uniformity.

using the equations in Ref. 13. Momentum-weighting β for the step size along φ was calculated based on Eq. [8a]. Wire segments were moved to the next iteration using Eqs. [7] and [9]. This process was repeated 20–30 times until the local minimum was reached under constraints, which took about 2 hr on an SGI Indigo2 workstation.

Figures 2 and 3 show the winding patterns for the *X* gradient without and with this technique, respectively. In Fig. 2, the efficiency was 1.52 mT · m^{-1} · A^{-1}, and the average error over a spherical volume of 7 cm diameter was 1.27%. The irregular winding patterns are apparent, especially in region *D* (see Fig. 2). These sharp inflections limit the number of wire loops that can be used, which in turn limits coil efficiency and degrades the uniformity of the gradient field. These irregular patterns do not disappear by increasing the number of wire segments. However, by using momentum-weighted step sizes and choosing small step sizes during the first iterations, as described above, the irregular winding patterns disappeared, which permitted more wire loops to be added, leading to improved coil efficiency and field uniformity. The efficiency of this coil is 2.13 mT · m^{-1} · A^{-1}, and the measured inductance is 199 μH. The *Y* gradient coil was designed in a similar fashion. The *Z* gradient coil was designed with two layers; Z_1 is the innermost layer with a total of 28 turns

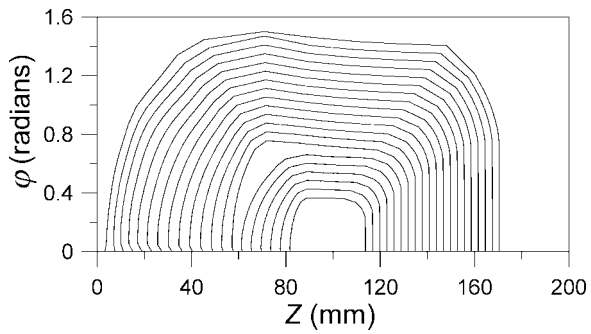

FIG. 3. Winding patterns based on the method of this article. The sharp inflections disappear, which permits 20 winding loops to be incorporated, resulting in designs with improved efficiency and gradient field uniformity.

Table 1
Specifications and Figure-of-Merit Values of the Rat Gradient Coil

Axis	Efficiency (mT · m^{-1} · A^{-1})	Inductance (μH)	Diameter (m)	*F* ($\times 10^{-4}$)
X (20 turns)	2.13	199	0.146	2.17
Y (20 turns)	2.08	202	0.152	2.33
Z_1 (28 turns)	2.08	67.7	0.139	3.32
Z_2 (36 turns)	2.03	119.3	0.158	3.26

of wires, and Z_2 is the outermost layer with 36 turns of wires. Table 1 lists the detailed coil specifications and the figure-of-merit values that were calculated using the formula proposed by Chronik et al. (17,18):

$$F = \frac{\eta \cdot a^{2.5}}{\sqrt{L}}, \qquad [10]$$

where η is the gradient efficiency (mT · m^{-1} · A^{-1}) within the region of interest, *L* is the coil inductance (μH), and *a* is coil radius (m). This definition of figure-of-merit assumes that inductance scales with the fifth power of radius (1). However, this has not been fully justified in real coil design situations. The *F* values for Z_1 and Z_2 are essentially the same, while they are similar for *X* and *Y* (see Table 1). These data suggest that Eq. [10] is suitable for quantifying the performance of a single-layer *Z* gradient coil, and that it is also reasonable for evaluating single-layer transverse gradient coils with a cylindrical geometry. However, this formula does not include gradient field linearity, uniformity, and coil length. Coil length can be an important parameter for human gradient coil design because of coil-shoulder clearance and magnetostimulation concerns.

Figure 4 shows the gradient coil that was constructed in our laboratory. Winding grooves for Z_1, *X, Y,* and Z_2 were cut layer by layer using a numerically controlled milling

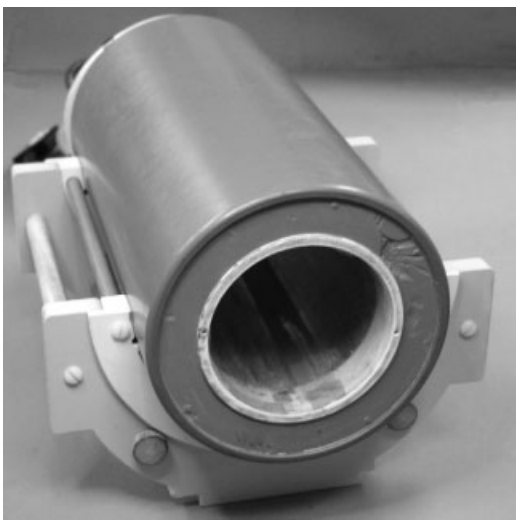

FIG. 4. Water-cooled, torque-balanced, three-axis gradient coil designed using the MW-CGD method. This coil has an efficiency of 2.13, 2.08, and 4.12 mT · m^{-1} · A^{-1} along *X, Y,* and *Z*, respectively, and is driven at 96 μs rise time.

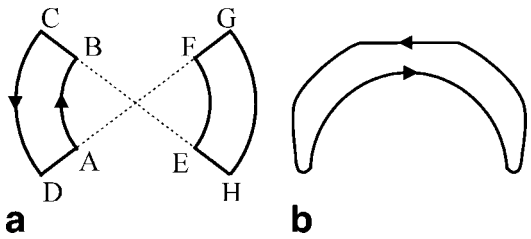

FIG. 5. **a:** Coil design using coaxial return paths. The active arc *AB* is shorter than the return arc *CD*. **b:** Coil design using remote current return paths (the other half is symmetric). The active and return arcs have different radius and azimuthal angles. Each wire loop is divided into 128 wire segments and each segment has three parameters (r, φ, z) to be optimized. As a result, the optimum outer surface of the wire loop is irregular and is different from loop to loop. These wire loops are embedded into disks and sandwiched together.

machine. Copper wires (AWG No. 13) were embedded in the grooves and stabilized with epoxy. Water-cooling was incorporated outside Z_2 using copper tubing. This coil is 12.8 cm I.D., 20 cm O.D., 35.6 cm in length, and weighs 19.8 kg.

Gradient Coil Design Using Remote Current Return Paths for Human Brain

Local gradient coils with low inductance, reasonable efficiency, easy access to the uniform gradient region of the coil, and low acoustic noise are desirable in MRI using human subjects. The use of coaxial return paths provides a good compromise that meets these requirements (9,19–21). Figure 5a shows two coaxial loops. The active arc *AB* is shorter than the return arc *CD*, and the radial elements *BC* and *DA* generate gradient fields that degrade field uniformity in the center of the coil. Instead of using the same azimuthal angles in the active and return arcs as in coaxial geometry, an approach employing remote current return paths has been suggested (2). In this approach, wire loops are embedded in planar disks and the disks are then sandwiched together. Each wire loop has 128 discrete wire segments, each with three parameters (r, φ, z) to be optimized. As a result, the optimum outer surface of the wire loops is irregular (see Fig. 5b for details). The MW-CGD method has been applied to design a "sandwich" gradient coil. This coil has 0.32 m I.D. and 0.45 m O.D., with an efficiency of 0.118 $mT \cdot m^{-1} \cdot A^{-1}$ and inductance of 310 μH. The total length of this coil is 0.29 m. The rms error over a cylindrical volume of 0.175 m diameter and 0.19 cm length is 3.1%. The figure-of-merit of this design is similar to that of equivalent designs using coaxial return paths (19,20), although the value of $\eta/\sqrt{L}$ is about 1.5–3 times greater than the latter two designs. One notable advantage in the sandwich gradient design is that the length-to-diameter ratio is only 0.92, which is about half of that in Refs. 19 and 20. This coil is under construction and experimental results will be reported in the future.

Rat Gradient Coil Evaluations

A 16-strut birdcage RF coil with 5.1 cm I.D. and a length of 9.5 cm was built to evaluate field uniformity and linearity of this gradient coil. All experiments were carried out on a 3T BIOSPEC 30/60 scanner (Bruker Medizintechnik, Karlsruhe, Germany). Figure 6a is a sagittal image acquired using a FLASH-type sequence with a homemade cylindrical phantom (4.8 cm I.D., 9.5 cm in length). Scan parameters were: TR 500 ms, TE 10.5 ms, FOV 12 cm, 2 mm slice thickness, matrix size 256 × 256, six averages. The maximum distortion measured 3.1 cm away from the center of the image was 2%, which agrees well with theoretical designs. The dark areas at the top and bottom of Fig. 6a were due to RF field nonuniformity close to the end-rings of the birdcage coil.

Figure 6b–d shows axial images acquired using a homemade grid phantom (4.8 cm I.D., 9.5 cm in length). The dimension of the grids was about 1.5 × 1.5 cm^2. Scan parameters were the same as for Fig. 6a except that the FOV was 6 cm. Three slices with a slice separation of 2.5 cm were acquired. No obvious distortions were observed in these images.

High-Resolution fMRI Using the Rat Gradient Coil

This coil was applied to fMRI experiments using a rat whisker-barrel stimulation model. α-chloralose anesthetized rats were paralyzed with gallamine and mechanically ventilated. The femoral artery and vein were cannulated for blood pressure monitoring, blood gas measurements, and drug delivery. The rectal temperature was maintained at 37 ± 0.5°C by a temperature-controlled water-heating pad. The rat head was fixed with a homemade bite bar and ear bar. A homemade saddle coil of 9 cm I.D. and 10 cm length was used for RF excitation with a 1.5 cm

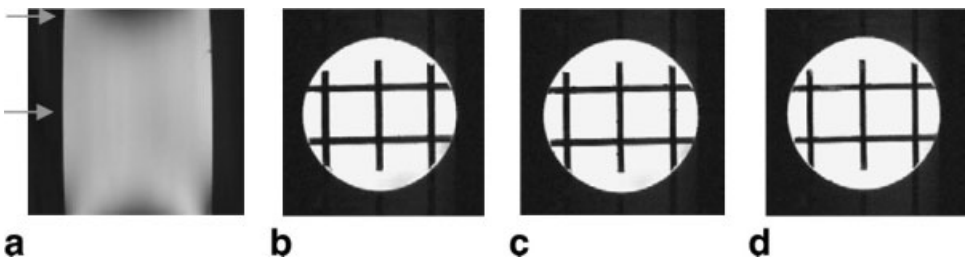

FIG. 6. Evaluations of the gradient coil. Image **a** was acquired using a cylindrical phantom. Arrows indicate the maximum distortions 3.1 cm away from the center of the gradient coil. The dark areas at the top and bottom of this image are due to RF field inhomogeneities at both ends of the birdcage coil. **b–d:** Axial images acquired using a homemade grid phantom. Image **c** was at the center of the gradient coil. Slice separation was 2.5 cm.

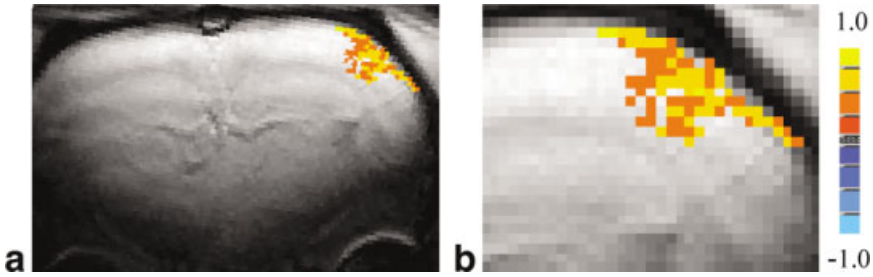

FIG. 7. High-resolution cross-correlation activation maps (voxel volume: 156 × 156 × 2000 μm^3). Left: activation map superimposed on the first EPI image in the time course. Right: enlarged view of the activation map in the whisker-barrel cortex. Data were acquired using two-shot partial *k*-space EPI. Scan parameters were: FOV = 2 cm, slice thickness = 2 mm, matrix size = 128 × 128, effective TR = 2 sec (1 sec per shot). The activated pixels are primarily located in the gray matter and the pixels with high BOLD responses (the yellow pixels in Fig. 7b) are located on the surface and deep cortical layers.

I.D. surface coil for signal reception. A homemade whisker stimulator was used to deliver stimulus of desired frequencies and durations. All animal protocols were approved by the Laboratory Animal Safety Committee of the Medical College of Wisconsin.

A two-shot, half *k*-space echo planar imaging (EPI) sequence with phase-corrected by phase-encoded calibration scans was used in this study (22). The scan parameters were: FOV 2 cm, matrix size 128 × 128, TE 24 ms, slice thickness 2 mm, data acquisition bandwidth 166 kHz, effective TR 2 sec (1 sec per shot). The scan paradigm was a block design consisting of four cycles of 64 sec on and 32 sec off. Functional data were analyzed using a cross-correlation method (23) in the AFNI software package (24). All pixels in the whisker-barrel cortex with a *P*-value $<$ 0.005 were considered activated.

Figure 7a shows a cross-correlation activation map superimposed on the first EPI image in the time course. Figure 7b is an enlarged view of the activation map in Fig. 7a. The activated pixels are primarily located in the gray matter and the pixels with high BOLD responses (the yellow pixels in Fig. 7b) are located on the surface and deep cortical layers. These data demonstrate that with this high-efficiency gradient coil we are able to acquire high-resolution fMRI data using reduced FOV with increased data acquisition bandwidth and reasonable temporal resolution (effective TR = 2 sec).

DISCUSSION

In gradient coil optimization using CGD, the constraints are more complicated for transverse gradient coils than for the *Z* gradient coil because of the greater number of elements and additional dimensions for each element. The Hessian matrix, which encodes the curvature information of the error function, has not been used in the past. The Levenberg-Marquardt algorithm takes curvature information into account by adjusting the step sizes in each direction using an estimated Hessian matrix. This method has been widely applied in the optimization of medium-sized nonlinear models. However, matrix inversion makes this method inefficient for transverse gradient coil design. Our method takes advantage of the efficiency of the CGD method combined with momentum weighting, which is an intrinsic property of the Levenberg-Marquardt algorithm, to adjust step sizes along the three orthogonal directions (r, φ, z). Like the Levenberg-Marquart algorithm, our approach is heuristic; however, it tends to generate practical designs with high efficiency and field homogeneity. Using the design pattern shown in Fig. 3, the efficiency increased by 40% over Fig. 2 and the field uniformity increased by 27%.

The major difference between our method and the original CGD method proposed by Wong et al. is the decomposition of Eq. [4] into Eqs. [7] and [8]. The major benefit of this method is higher efficiency in a single-layer gradient coil. One tradeoff is that higher efficiency usually results in more compact wire patterns, leading to increased coil inductance. In practice, the inductance in a single-layer gradient coil of the size described here is not a major concern. However, power consumption is a serious concern in small-sized gradient coils. High efficiency can, to some extent, alleviate power consumption problems, since for a given gradient strength, the current is inversely proportional to the efficiency η, and power consumption is approximately proportional to $1/\eta^2$. In this implementation, we were motivated to design a high-efficiency gradient coil for high-resolution fMRI and no constraints on inductance and power were included. If inductance and power need to be optimized the error function in Eq. [2] can be modified to include them with proper weightings, as described by Wong et al. (3). However, in this case gradient uniformity and efficiency are generally compromised (1,3).

Spatial resolution, temporal resolution, and signal-to-noise ratio (SNR) are limiting factors in fMRI. Single-shot EPI has been widely applied in fMRI for high temporal resolution imaging. However, the spatial resolution is limited due to T_2^* decay. *K*-space interleaving can improve spatial resolution but compromises temporal resolution (25). With this high-efficiency gradient coil, we were able to decrease the FOV while increasing data acquisition bandwidth. Smaller FOV allows fewer *k*-space lines to be acquired for a given resolution, which improves temporal resolution; higher data acquisition bandwidth permits shorter data acquisition times, which reduces distortion with improved SNR. Half *k*-space EPI permits short TE, which further improves the SNR. Using this gradient coil combined with a two-shot half *k*-space EPI sequence, we have detected BOLD response at a resolution of 156 ×

$156 \times 2000\ \mu m^3$ with a temporal resolution of 2 sec, as shown in Fig. 6, which would otherwise be very difficult to obtain without this high gradient strength.

For gradient coil design under the same conditions, the analytical methods and the numerical optimization methods should ideally result in the same solution. The major advantage of the numerical optimization method is the flexibility of working in real space (instead of Fourier space) without strong geometric constraints. These methods are suitable for designing coils of irregular geometries, very few turns of wire, and very short dimensions, such as the sandwich gradient coil.

ACKNOWLEDGMENTS

The authors thank Drs. Robert W. Cox at NIH and Gaohong Wu and Daniel B. Rowe at the Medical College of Wisconsin for valuable discussions. Richard Johnson, Richard Scherr, and Michael Rudzik helped in construction of the gradient coil.

REFERENCES

1. Turner R. Gradient coil design: a review of methods. Magn Reson Imag 1993;11:903–920.
2. Lu H, Jesmanowicz A, Li S-J, Hyde JS. Short gradient coil design using efficiency-optimized remote current return paths. In: Proc 9th Annual Meeting ISMRM, Glasgow, 2001. p 613.
3. Wong EC, Jesmanowicz A, Hyde JS. Coil optimization for MRI by conjugate gradient descent. Magn Reson Med 1991;21:39–48.
4. Buszko ML, Kempka MF, Szczesniak E, Wang DC, Andrew ER. Optimization of transverse gradient coils with coaxial return paths by simulated annealing. J Magn Res 1996;112(B):207–213.
5. Fisher BJ, Dillon N, Carpenter TA, Hall LD. Design of a biplanar gradient coil using a genetic algorithm. Magn Reson Imag 1997;15:369–376.
6. Crozier S, Doddrell DM. Gradient-coil design by simulated annealing. J Magn Reson 1993;103(A):354–357.
7. Crozier S, Forbes LK, Doddrell DM. The design of transverse gradient coils of restricted length by simulated annealing. J Magn Reson 1994; 107(A):126–128.
8. Tomassi D, Caparelli EC, Panepucci H, Foerster B. Fast optimization of a biplanar gradient coil set. J Magn Reson 1999;140:325–339.
9. Brey WW, Mareci TH, Dougherty J. A field-gradient coil using concentric return paths. J Magn Res 1996;112(B):124–130.
10. Mao J, Mareci TH, Scott KN, Andrew ER. Selective inversion radiofrequency pulses by optimal control. J Magn Res 1986;70:310–318.
11. Pruessman KP, Weiger M, Bornert P, Boesiger P. Advances in sensitivity encoding with arbitrary k-space trajectories. Magn Reson Med 2001; 46:638–651.
12. Lu H, Jesmanowicz A, Hyde JS. A technique for Hessian matrix formation for gradient coil optimization. In: Proc 10th Annual Meeting ISMRM, Honolunu, 2002. p 813.
13. Press WH, Teukolsky SA, Vetterling WT, Flannery BP. Numerical recipes in C. New York: Cambridge University Press; 1992. p 412–424, p 681–685.
14. Hagan MT, Demuth HB, Beale M. Neural network design. Boston: PWS Publishing; 1996. p 19–31.
15. Levenberg K. A method for the solution of certain problems in least squares. Q Appl Math 1944;2:164–168.
16. Marquardt D. An algorithm for least-squares estimation of nonlinear parameters. SIAM J Appl Math 1963;11:431–441.
17. Chronik BA, Alejski A, Rutt BK. Design and fabrication of a three-axis edge ROU head and neck gradient coil. Magn Res Med 2000;44:955–963.
18. Chronik BA, Rutt BK. Constrained length minimum inductance gradient coil design. Magn Res Med 1998;39:270–278.
19. Mansfield P, Chapman BLW, Bowtell R, Glover P, Coxon R, Harvey PR. Active acoustic screening: reduction of noise in gradient coils by Lorentz force balancing. Magn Reson Med 1995;33:276–281.
20. Bowtell R, Peters A. Analytical approach to the design of transverse gradient coils for co-axial return paths. Magn Reson Med 1999;41:600–608.
21. Chapman BLW, Mansfield P. A quiet gradient-coil set employing optimized, force-shielded, distributed coil designs. J Magn Res 1995;107: 152–157.
22. Lu H, Jesmanowicz A, Mazaheri Y, Hyde JS. Reference scan navigator-aided half k-space interleaved EPI for high resolution fMRI at 3T. In: Proc 10th Annual Meeting ISMRM, Honolulu, 2002. p 2372.
23. Bandettini PA, Jesmanowicz A, Wong EC, Hyde JS. Processing strategies for time-course data sets in functional MRI of the human brain. Magn Reson Med 1993;30:161–173.
24. Cox RW, Hyde JS. Software tools for analysis and visualization of fMRI data. NMR Biomed 1997;10:171–178.
25. McKinnon GC. Ultrafast interleaved gradient-echo-planar imaging on a standard scanner. Magn Reson Med 1993;30:609–616.